THE UNIVERSITY OF CHICAGO

MASTER'S THESIS

Separating Neutrino-less Double Beta Decay from Solar Neutrino Interactions in a Large Liquid Scintillator Detector with Spherical Harmonics

---

Author:
Runyu JIANG

Supervisors:
Andrey ELAGIN & Henry FRISCH

A thesis submitted in fulfillment of the requirements
for the degree of Master of Science

in the

Physical Sciences Division

August 17, 2018

Abstract

Separating Neutrino-less Double Beta Decay from Solar Neutrino Interactions in a Large Liquid Scintillator Detector with Spherical Harmonics

The elastic scattering of the ^{8}B solar neutrinos becomes one of the dominant backgrounds in the searches for neutrino-less double beta decay with a large liquid scintillator detector. We have improved a previously published technique that uses spherical harmonics analysis of the early photo-electrons to extract the topological differences between the ^{130}Te neutrino-less double beta decay signal from the ^{8}B solar neutrino interaction background. Similar to the previous work we evaluate the performance of the new method by using a simulation of a 6.5 m radius ^{130}Te-loaded liquid scintillator detector with the scintillation properties similar to KamLAND-Zen and surrounded by the photo-detectors with a 100 ps time resolution. The improved spherical harmonics analysis, supplemented by a maximum likelihood method, outperforms the earlier technique in the background suppression by 15%, for the events located at the center of the detector. For the events uniformly distributed throughout the 3 m radius fiducial volume, we achieve 30% improvement: we demonstrate a factor of 2.6 in ^{8}B background suppression at 70% signal efficiency which is to be compared with the previous factor of 2 in the ^{8}B background suppression at the same signal efficiency. This new level of the background suppression was previously achieved only by increasing the risetime of the scintillation light from 1 ns to 5 ns. We have also reduced the computation run time by more than 200 times. The improvements in the new method comes from harnessing the spacetime coordinates of each individual photoelectron, modifying the integral into a summation to perform the spherical harmonics analysis, and suppressing the weights on the photoelectrons from the scintillation light. Additionally, we have completed the first simulation studies demonstrating the direction reconstruction of the 2.5 MeV electrons in a liquid scintillator detector for events uniformly distributed in the R<3 m fiducial volume. The reconstruction of the electron direction is important to further suppress the ^{8}B background in the off-center events by correlating the electron direction with the position of the sun. We have also started developing potential vertex reconstruction technique using the photoelectrons from the early scintillation light, supplementary to the previous vertex reconstruction technique based on the early Cherenkov light, which has a possibility to further improve the accuracy of the vertex reconstruction.

Acknowledgements

I would like to first thank my mother J. Xu and my father L. Jiang for their love.

I would like to thank my thesis advisor Andrey Elagin. He has been consistently encouraging me and helping me throughout the entire research project. He has also been sharing his experience in the countless technical details of the codes. He is the one who first noticed the fact that the previous integral method and the current summation method lead to similar results of the spherical harmonics spectra, which initiates and motivates my investigation. He is also the one who suggested harnessing the position of the Sun to further separate those off-center signal events, which are falsely classified as background events, from the true backgrounds.

I would also like to thank my thesis advisor Henry Frisch. He has been consistently giving me insightful feedbacks to my group meeting reports and providing helpful suggestions on my thesis writing. He is the one who guides me to the research of high energy physics experiment. He has also shared a novel potential method to separate the Cherenkov light from the scintillation light, which motivates my further study on the light separation.

I would like to acknowledge Chuck Whitmer. He has been responding to the new techniques in the project very quickly, and has been consistently asking insightful questions and providing brilliant suggestions accordingly. He has also implied the partition of the sphere over $(\cos\theta, \phi)$ is better than over (θ, ϕ), as the former partition leads to a more uniform area assignment to each grid, which motivates me to plot the most diagrams with $cos\theta$ instead of θ. In addition, he is very knowledgeable and has been sharing his knowledge in physics and computer science, which is impressive and has a great positive impact on me.

I also want to acknowledge Roy Garcia. He is a great listener and his great passion has a very positive impact on me. He really loves the maths aspect in my project, and he always organizes a detailed note in his laptop while listening to my explanations. He also spontaneously constructed an animated display of the photo-electron hits for a simulated event, which provides an very intuitive picture of the event.

I want to acknowledge Evan Angelico. He is the one who patiently introduced the principle of the large-area picosecond photodetector (LAPPD), explained the detailed structure of the LAPPD and introduced the previous research on optical time projection chamber to me in detail.

I would like to acknowledge Eric Spieglan. He has been consistently sharing his experience in the lab, which largely enhanced my understanding and constructed my intuition on the physical realization of the LAPPD.

I would like to acknowledge Mary Heintz. She has been consistently protecting and maintaining the PSEC servers. She has also been providing her experience in technical support on the PSEC machines.

I would like to acknowledge Jim Pilcher. He has been administrating and supervising the MSPSD program. He has been patiently providing helpful suggestions on the course selection and the advisor information on the master research.

I would like to acknowledge Emily Easton. She has been managing and organizing the MSPSD events. She has also been very supportive and very efficient, which guarantees my program goes smoothly.

I would like to acknowledge Christian Ferko. He has been consistently providing helpful suggestions on the course selection and research project. He has also been organizing the MSPSD events, which has a positive impact on me.

Contents

Chapter 1

Introduction

1.1 Introduction

An important missing ingredient in the Standard Model of particle physics is the answer to a question on whether the neutrino is its own antiparticle, i.e. is the neutrino a Majorana particle [1]. The neutrino carries no electric charge and therefore it is the only fermion in the standard model for which it is possible to be a Majorana particle. It is not only possible, but it could also be necessary to explain the matter-antimatter asymmetry [2] or to explain why the neutrino mass is so tiny comparing to all other fermions [3].

Searching for neutrinoless double-beta decay ($0\nu\beta\beta$-decay) [4, 5] is the most feasible experimental technique to determine if the neutrino is a Majorana particle. Neutrinoless double-beta decay $(Z, A) \rightarrow (Z+2, A) + 2e^-$ violates electron lepton number by two units and therefore has a potential to probe physics beyond the standard model [6]. At the same time, according to the Schechter-Valle theorem [7], the observation of $0\nu\beta\beta$-decay would guarantee the existence of a non-zero Majorana mass term for the neutrino[1].

If it exists, $0\nu\beta\beta$-decay is a very rare process with half-lifetime of $T_{1/2} > 10^{27}$ years. It can only be observed by taking the advantage of the large value of Avogadro's number. Due to the increasingly large experimental limits on $0\nu\beta\beta$-decay half-lifetime [9, 10, 11] all the currently planned experiments are aiming for a ton-scale of an active isotope mass [12]. A kilo-ton scale active isotope mass detector may be required to explore a well motivated region in the $0\nu\beta\beta$-decay parameter space [13].

Background suppression is a key criteria in designing any $0\nu\beta\beta$-decay experiment. The use of clean materials helps to reduce the backgrounds from the radioactive decays inside the detector. A shielding helps to reduce external backgrounds. A good energy resolution is essential to suppress two neutrino double-beta decay.

The scalability, self-shielding, and good energy resolution of the liquid scintillator detectors makes them a competitive option to the search for $0\nu\beta\beta$-decay [10]. However, in a kilo-ton scale liquid scintillator detector, the electrons from the elastic scattering of ^{8}B solar neutrino becomes a new dominant background [14].

This background events due to ^{8}B solar neutrino interactions cannot be reduced by measuring the total energy because ^{8}B events can have exactly the same energy as $0\nu\beta\beta$-decay signal events. In a liquid scintillator, ^{8}B background can be suppressed, if the Cherenkov light can be separated from the scintillation light to reconstruct the event topology [15], because ^{8}B background events have only one electron in the final state while $0\nu\beta\beta$-decay signal events have two electrons.

The cases, where the $0\nu\beta\beta$-decay signal events have only one electron above Cherenkov threshold or have two electrons emitted at a very small angle, the ^{8}B background still can be suppressed by reconstructing the electron directionality in a $0\nu\beta\beta$-decay candidate event [16, 13, 17, 18]. The events, where electron direction is consistent with the ^{8}B solar neutrino direction, can be rejected or assigned a lower weight when counting total number of $0\nu\beta\beta$-decay candidate events.

The Cherenkov threshold for an electron in a typical liquid scintillator is ~0.16 MeV. Therefore, the electrons produced in $0\nu\beta\beta$-decays and the electrons scattered in ^{8}B solar neutrino interactions can exceed the threshold and generate Cherenkov radiation. While emitting Cherenkov radiation, the most kinetic energy of the electrons above the threshold is transferred into the ionization energy of the liquid scintillator;

---

[1] For a "natural" gauge theory without an extreme fine tuning [7]. See also the Ref. [8] for more discussion on the Schechter-Valle theorem.

therefore, the kinetic energy of the electron drops rapidly below the Cherenkov threshold. The liquid scintillator gets excited by the ionization and by the absorption of a large proportion of the Cherenkov photons. As opposed to the Cherenkov light, the scintillation light is emitted isotropically. The scintillation light is abundant and lasts for ∼50 ns, while the Cherenkov light is prompt and lasts for ∼3.5 ns.

The separation of the Cherenkov light from the scintillation in a liquid scintillator detector for the $0\nu\beta\beta$-decay searches is an actively developing field [17, 15, 19, 19, 20]. In this work, we use simulation[2] to study the Cherenkov/scintillation light separation to reconstruct the event topology of the $0\nu\beta\beta$-decay events in a liquid scintillator detector similar to the KamLAND-Zen experiment. In our simulation taken from the Refs. [17, 15], the geometry of liquid scintillator volume (a sphere with R=6.5 m), fiducial volume (a sphere with R=3 m), the quantum efficiency (QE) of photo-detectors, and the scintillation properties match the KamLAND-Zen detector. Contrary to the KamLAND-Zen, we consider the ^{130}Te isotope loading instead of the ^{136}Xe at the KamLAND-Zen, a 100% photo-coverage instead of 34%, and a 100 ps time resolution of the photo-detectors instead of ∼1.5 ns [3].

The photo-detectors such as the Large-Area Picosecond Photodetectors (LAPPD) with a single photo-electron (PE) time resolution of <50 ps [23] can be used to separate the Cherenkov PEs from the scintillation PEs. The directionality of the Cherenkov PEs can be used to reconstruct the event topology and separate the $0\nu\beta\beta$-decays from the ^{8}B solar neutrino interactions. The isotropic scintillation PEs are still essential for the energy reconstruction.

As has been shown in the Ref. [15], the spherical harmonics analysis of the PEs spatial distribution provides the handles to separate the $0\nu\beta\beta$-decay signal from the ^{8}B background events. We have improved the technique from the Ref. [15] by harnessing the angular coordinates (θ, ϕ) and the arrival time t of each individual PE, assigning weights $W(\theta, t)$ to the PE's and replacing the integral (based on Monte Carlo integration method) with a summation to calculate the spherical harmonics power spectrum (S-spectrum) S_ℓ.

In the events with the vertices at the center of the detector sphere (central events), we have selected the photons arriving within the first 2ns with respect to the earliest photon to calculate the S-spectrum S_ℓ. We have achieved a background suppression factor of 5.2 at 70% signal efficiency, which is in comparison to the background suppression factor of 4.5 in the previous research [15].

In the events with the vertices randomly generated uniformly throughout the fiducial volume with 3m radius (off-center events), the photons are assigned weights $W(\theta, t)$ to calculate the S-spectrum S_ℓ. We have demonstrated a background suppression factor of 2.6 at 70% signal efficiency. This new level of the background suppression was previously achieved only by increasing the risetime of the scintillation light from 1 ns to 5 ns. In the off-center events without any change of the scintillator risetime, the previous research [15] demonstrated a background suppression factor of 2.0 at 70% signal efficiency .

The improved spherical harmonics analysis has improved the computation speed by more than a factor of 200, because the summation form of the S-spectrum has simplified the calculation of the two-dimensional integrals.

In addition, we have completed the first simulation studies demonstrating the direction reconstruction of the 2.5 MeV electrons in a liquid scintillator detector for events uniformly distributed in the R<3 m fiducial volume. Supplementary to using only event topology, reconstructing the electron direction and correlating the electron direction with the position of the sun may help to further suppress the ^{8}B background in the off-center events. In a true ^{8}B background event, the direction of the electron is correlated to the direction of the Sun-Earth connection $\hat{e}_{SE}$. However, in a $0\nu\beta\beta$-decay that is falsely classified as a ^{8}B background, the reconstructed direction of the electron has an isotropic angular probability density. Such difference in the angular probability distribution makes those events, which have the reconstructed electron direction $\hat{e}_{electron}$ opposite to the Sun-Earth connection $\hat{e}_{SE}$, more likely to be a $0\nu\beta\beta$ signal which was falsely classified as a ^{8}B background, based just on the event topology.

---

[2] Computational resources to simulate a total of 800,000 signal and background events and run various modifications of our reconstruction algorithms was provided by the Open Science Grid [21, 22], which is supported by the National Science Foundation award 1148698, and the U.S. Department of Energy's Office of Science.

[3] These detector parameters are chosen for consistency with Ref. [17, 15].

We have also started developing a potential vertex reconstruction scheme: reconstructing the vertex displacement direction $\hat{r}_v$ based on the reconstruction of the center of the mass of the early scintillation photon hits; and reconstruct the vertex displacement length r_v, based on the reconstruction of the time boundary $t_{cut}(\theta)$, which also separates the Cherenkov photons from the scintillation photons in the off-center events.

Chapter 2

Spherical harmonics analysis

Given an arbitrary event in the spherical liquid scintillator detector, the normalized angular density distribution $f(\theta, \phi)$ represents the total angular density distribution of the photo-electrons (PE) detected over the detector sphere:

$$f(\theta, \phi) = \sum_{i}^{N_{PE}} \frac{\delta(\theta - \theta_i)\delta(\phi - \phi_i)}{N_{PE} \sin\theta_i} \tag{2.1}$$

where N_{PE} is the total number of photo-electrons; θ_i and ϕ_i are the angular coordinates where each individual photo-electron is located.

Given any such detection signal $f(\theta, \phi)$, its S-spectrum S_ℓ is defined to be the sum of the square of the individual spherical harmonics expansion coefficients $f_{\ell m}$. Thanks to the expression of the detection signal $f(\theta, \phi)$, which is a sum of the Dirac delta functions, the integral in the expression of the coefficients $f_{\ell m}$ can be further simplified to be (see Equation A.6 for the detailed derivation):

$$S_\ell = \sum_{m=-\ell}^{\ell} |f_{\ell m}|^2 = \frac{1}{N_{PE}^2} \sum_{m=-\ell}^{\ell} \left| \sum_{i=1}^{N_{PE}} Y_{\ell m}(\theta_i, \phi_i) \right|^2 \tag{2.2}$$

where $f_{\ell m}$ is the individual spherical harmonics expansion coefficient; the special function $Y_{\ell m}(\theta, \phi)$ is the tesseral harmonics (real-valued spherical harmonics).

The simplified expression of the S-spectrum S_ℓ is a sum instead of an integral; therefore, given the same amount of time, computers are able to calculate many more S_ℓ's with much larger ℓ's. Consequently, one can practically plot the corresponding S-spectrum S_ℓ as a function of ℓ.

2.1 Central Events

The Central events are the events with their vertices located at the center of the liquid scintillator detector sphere. Because of the 1ns risetime of the scintillation photons, the Cherenkov photons in the central events always arrive earlier than the scintillation photons at the detector sphere. Therefore, the most photons from the first 1ns time bin (with respect to the time of the first photo-electron) are Cherenkov photons (see Figure 2.1).

By spherical harmonics analysis, the S-spectrum S_ℓ of the angular density distribution $f(\theta, \phi)$ of the selected PE's from the first 1ns determines whether the event is a $0\nu\beta\beta$-decay or a solar neutrino interaction. The difference between the S-spectrum S_ℓ of the signal events ($0\nu\beta\beta$) and the background events (solar neutrino interaction) is illustrated in the Figure 2.2

As shown in the Figure 2.2, the expectation of S_1 of the signal ($0\nu\beta\beta$) is smaller than S_1 of the background (solar neutrino interaction). Additionally, we can read the slope α and the intersection β from the S-spectrum by applying linear regression $S_\ell = \alpha\ell + \beta$. The expectation of the slope α of the signal is larger than the slope α of the background. The histogram of S_1 and the histogram of the slope α are given in the Figure 2.3.

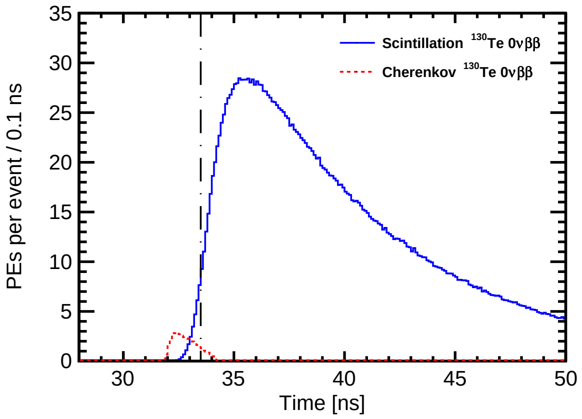

Figure 2.1: Figure taken from the Ref. [15]: the arrival time distribution of the photons in the central events. [*Red*]: The Cherenkov arrival time distribution in the central events. [*Blue*]: The scintillation arrival time distribution in the central events. This diagram shows, in the central events, the most Cherenkov photons always arrive earlier than the most scintillation photons. Therefore, one can increase the proportion of the Cherenkov photons and suppress the proportion of the scintillation photons, by introducing a time cut.

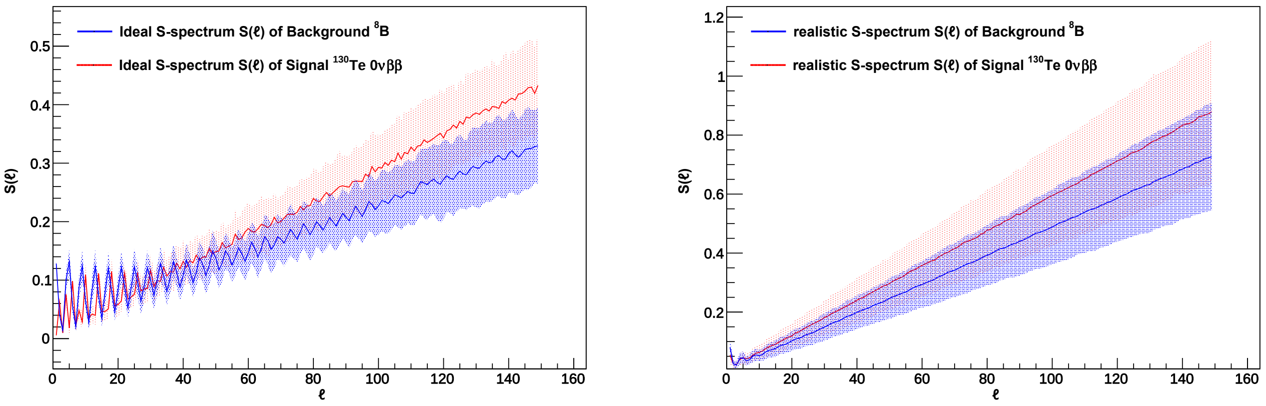

Figure 2.2: The S-spectrum S_ℓ in the central events, as a function of ℓ. Each individual event has its unique S-spectrum S_ℓ, which varies from event to event. The shaded area represents the error bar of each S_ℓ. [*Left*]: The event-averaged S-spectrum S_ℓ of the angular distribution $f(\theta, \phi)$ of all the photo-electrons from the first 1ns time bin (with respect to the first detected photon) of the signals ($0\nu\beta\beta$ events, *red*) and the backgrounds (^{8}B solar neutrino interaction events, *blue*) in the ideal cases simulated with only the Cherenkov photons, a 30% of quantum efficiency and no multiple scattering. [*Right*]: The event-averaged S-spectrum S_ℓ of the angular distribution $f(\theta, \phi)$ of all the photo-electrons from the first 1ns time bin (with respect to the first detected photon) of signals ($0\nu\beta\beta$ events, *red*) and the backgrounds (^{8}B solar neutrino interaction events, *blue*) in the realistic cases. In general, the signal events have smaller S_1's than the background events. Also, the signal events generally have larger S-spectrum slopes α than the background events.

2.2 Separation of Cherenkov photons from the scintillation photons

In the events with the vertices uniformly randomly located within the entire fiducial volume (ball with 3m radius) of the liquid scintillator detector, the Cherenkov photons do not necessarily arrive earlier than the scintillation photons. For example, consider an event with its vertex displaced from the center of the liquid scintillator detector, the direction of the electron(s) in this event could point from the vertex, towards the farther side of the sphere. Meanwhile, the scintillation photons always emit isotropically from the vertex, towards all of the directions, including the closer side of the sphere. As a consequence, the scintillation photons may arrive earlier than the Cherenkov photons in this particular example.

However, for any given infinitesimal segment on the sphere, regardless of the type of the event, the Cherenkov photons must arrive earlier than the scintillation photons, if there is any Cherenkov photon propagating towards this segment on the sphere. Equivalently, for any given individual detector at an angle (θ, ϕ) on the sphere, the Cherenkov photons must arrive earlier than the scintillation photons, if there is any Cherenkov photon propagating towards this detector.

Furthermore, we proposed a novel method (See Figure D.1) to reconstruct the unit vertex displacement vector $\hat{r}_v$ from the center of the detector sphere, using the center of mass of the scintillation photon hits (See Figure D.1). On top of the vertex displacement direction, we can reconstruct the entire vertex displacement

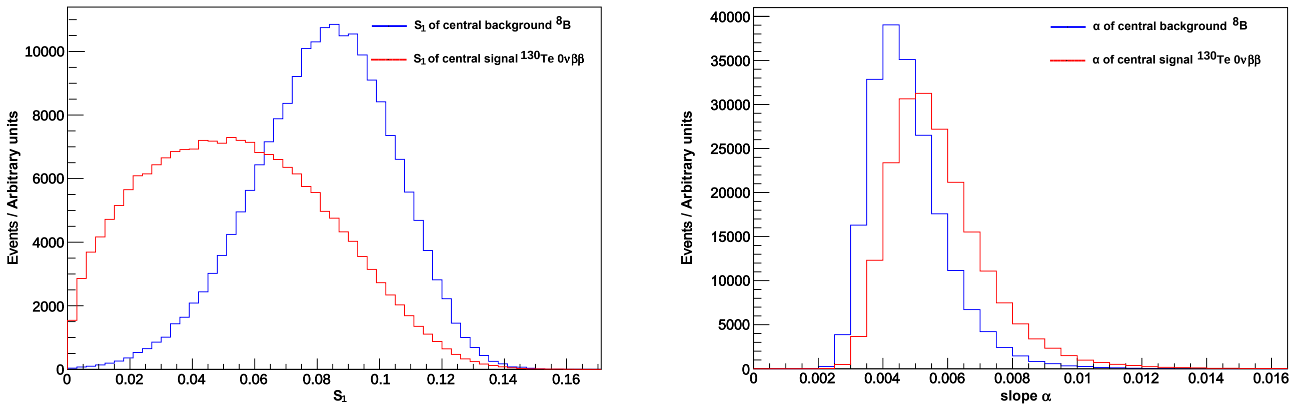

Figure 2.3: The parameters S_1 and α are extracted from the S-spectrum with the photon hits from the first 1ns with respect to the earliest detected photon hit in the central events. [*Left, red*]: The S_1 histogram of the signal ($0\nu\beta\beta$), which is proportional to the conditional probability distribution $p(S_1|1e)$. [*Left, blue*]: The S_1 histogram of the background (solar neutrino interaction), which is proportional to the conditional probability distribution $p(S_1|2e)$. [*Right, red*]: The histogram of the S-spectrum slope α of the signal($0\nu\beta\beta$), which is proportional to the conditional probability distribution $p(\alpha|1e)$. [*Right, blue*]: The histogram of the S-spectrum slope α of the background (solar neutrino interaction), which is proportional to the conditional probability distribution $p(\alpha|2e)$. This two diagrams illustrate the differences in S_1 and α between signal central events and background central events

vector $\vec{r}_v$ (which also includes the length r_v on top of the direction $\hat{r}_v$) from the center of the detector sphere using early Cherenkov photons in our previous research.

Therefore, the z-axis of the spherical coordinate can be defined to be aligned with the reconstructed direction of the vertex displacement vector from the center. In such coordinate system, for each given angle θ (regardless of ϕ), the Cherenkov photons always arrive earlier than the scintillation photons, which is illustrated in the Figure 2.4.

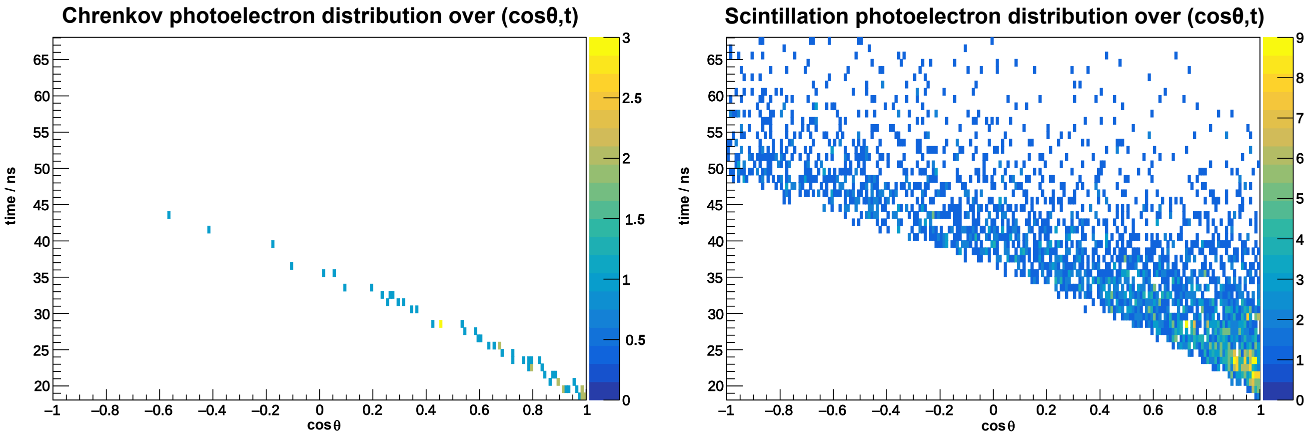

Figure 2.4: Aligning the z-axis with the direction of the vertex displacement vector from the center, all the photon hits are plotted according to their angle positions θ on the detector sphere and the arrival time t with respect to the earliest photon. [*Left*]: the number density of the Cherenkov photons $N_{Ch}(\cos\theta, t)$ plotted over $\cos\theta$ and t. [*Right*]: the number density of the scintillation photons $N_{Sc}(\cos\theta, t)$ plotted over $\cos\theta$ and t. These two diagrams show explicitly that, if we define the z-axis to be aligned with the vertex displacement direction $\hat{r}_v$, for any given angle θ, the Cherenkov photons always arrive earlier than the scintillation photons.

The time boundary $t_{cut}(\theta)$ with respect to the arrival time of the earliest photon, as a function of the angle θ, that separates the Cherenkov photons from the scintillation photons, is given by:

$$t_{cut}(\theta) = \frac{\sqrt{R^2 + r_v^2 - 2Rr_v\cos\theta}}{c(n)} - \frac{R - r_v}{c(n)} + t_{above} \tag{2.3}$$

where, R is the radius of the liquid scintillator detector; r_v is the length of the vertex displacement vector from the center; $c(n)$ is the speed of light in the liquid scintillator; t_{above} is the uncertainty of the exact boundary, which is usually arround 1ns.

The uncertainty term t_{above} arises from the ignorance of the type of the first detected photon, which could be either a Cherenkov photon or a scintillation photon. If the first detected photon is a scintillation photon, t_{above} will be 0. If the first detected photon is a Cherenkov photon, t_{above} will be the time difference of this earliest Cherenkov photon is and the earliest scintillation photon. Intuitively, the time boundary t_{cut} should translate upwards by t_{above} according to how early the first Cherenkov photon is, with respect to the scintillation photon. Such uncertainty t_{above} will be irrelevant, if we assign a weight $W(\theta, t)$ (proportional to an exponential function of $-t$) to each individual photon, according to how early the individual photon is with respect to the boundary.

In addition, given the vertex displacement direction $\hat{r}_v$, which is easier to reconstruct, the time boundary $t_{cut}(\theta)$ can be reconstructed without the knowledge of the vertex displacement length r_v. The earliest scintillation photons at each angle θ defines the time boundary $t_{cut}(\theta)$, which is a parametric function of θ depending on the parameter r_v. Therefore, not only using the early Cherenkov photons in the previous research, but also the early scintillation photons can also be useful to reconstruct the vertex $\vec{r}_v$. Using both the early Cherenkov photons and the early scintillation photons may potentially achieve a better accuracy of the reconstructed vertex.

2.3 Weight assignment function

Based on the separation (See Figure 2.4) of the (θ, t) distribution of the Cherenkov photons and scintillation photons, a weight assignment $W(\theta, t)$ on each individual photon hit $\frac{\delta(\theta-\theta_i)\delta(\phi-\phi_i)}{\sin\theta_i}$ at time t_i according to how early the photon arrives with respect to the time boundary $t_{cut}(\theta)$, can significantly increase the total weight on the Cherenkov photons, and suppress the total weight on the scintillation photons. In this paper, the weight assignment $W(\theta, t)$ is defined to be:

$$W(\theta, t) = exp\left[\frac{\frac{\sqrt{R^2+r_v^2-2Rr_v\cos\theta}}{c(n)} - \frac{R-r_v}{c(n)} + t_{above} - t}{\tau}\right] \tag{2.4}$$

where t is the photon arrival time with respect to the earliest photon; τ is a time constant which is defined to be $0.4ns$.

Given any angle θ, the difference between the arrival time of the Cherenkov photons and scintillation photons is fixed (For example, see Figure 2.1). Therefore, regardless how big the uncertainty t_{above} is, the weight of the first Cherenkov photon, relative to the weight of the first scintillation photon is fixed. Consequently, the total weight on all the Cherenkov photons relative to the total weight on all the scintillation photons is robust against the ignorance of the uncertainty t_{above}.

2.4 Off-center events

The off-center events are defined to be the events with the vertices randomly located within the fiducial volume of the liquid scintillator detector. In the off-center events, the normalized S-spectrum S_ℓ is modified based on the weight assignment function $W(\theta, t)$ defined in the Equation 2.4.

$$S_\ell = \sum_{m=-\ell}^{\ell} |f_{\ell m}|^2 = \sum_{m=-\ell}^{\ell} \frac{\left|\sum_{i=1}^{N_{PE}} W(\theta_i, t_i) Y_{\ell m}(\theta_i, \phi_i)\right|^2}{\left|\sum_{i=1}^{N_{PE}} W(\theta_i, t_i)\right|^2} \tag{2.5}$$

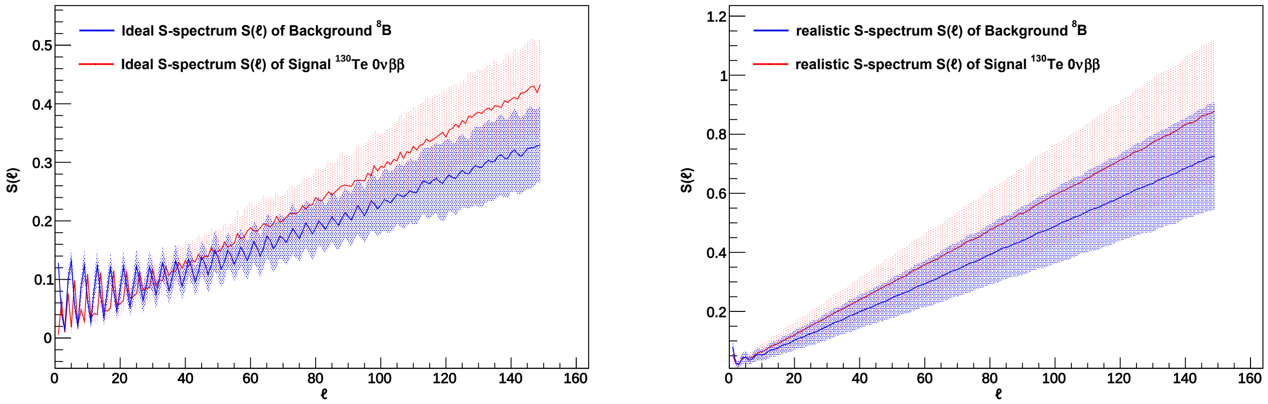

Figure 2.5: The S-spectrum S_ℓ in the off-center events, as a function of ℓ. Each individual event has its unique S-spectrum S_ℓ, which varies from event to event. The shaded area represents the error bar of each S_ℓ. [*Left*]: The event-averaged S-spectrum S_ℓ of the weighted angular distribution $f(\theta,\phi)$ of all the photo-electrons of the signals ($0\nu\beta\beta$ events, *red*) and the backgrounds (^{8}B solar neutrino interaction events, *blue*) in the ideal cases simulated with only the Cherenkov photons, a 30% quantum efficiency and no multiple scattering. [*Right*]: The event-averaged S-spectrum S_ℓ of the weighted angular distribution $f(\theta,\phi)$ of all the photo-electrons of the signals ($0\nu\beta\beta$ events, *red*) and the backgrounds (^{8}B solar neutrino interaction events, *blue*) in the realistic cases. In general, the signal events have smaller S_1's than the background events. Also, the signal events generally have larger S-spectrum slopes α than the background events.

Despite the modification of including the weight, $W(\theta,t)$ the off-center event classification is very similar to the central event classification: signal events have a larger expectation of S_1 and a smaller expectation of the S-spectrum slope α. Therefore, S_1 and the slope α of the S-spectrum determines the likelihood for the off-center event to be a signal and the likelihood for the off-center event to be a background.

Furthermore, applying the weight assignment function $W(\theta,t)$ to the central event classification has the result consistent with the method of not applying the weight assignment; therefore, the central event classification are generalized to the events that have the vertices located within the fiducial volume of the liquid scintillator. The central event classification becomes just a special case of the generalized off-center event classification.

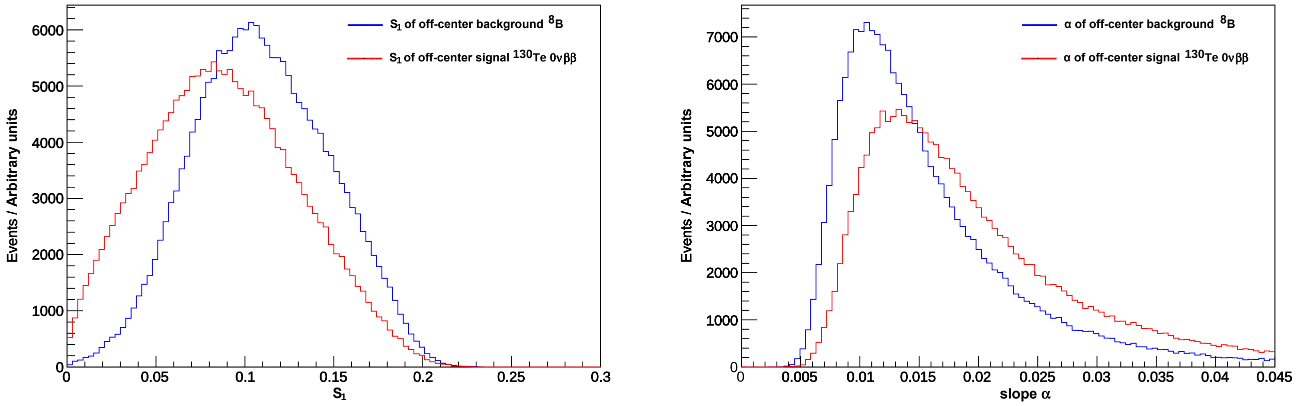

Figure 2.6: The parameters S_1 and α are extracted from the S-spectrum with the weighted photon hits in the off-center events. [*Left, red*]: The S_1 histogram of the signal ($0\nu\beta\beta$), which is proportional to the conditional probability distribution $p(S_1|1e)$. [*Left, blue*]: The S_1 histogram of the background (solar neutrino interaction), which is proportional to the conditional probability distribution $p(S_1|2e)$. [*Right, red*]: The histogram of the S-spectrum slope α of the signal($0\nu\beta\beta$), which is proportional to the conditional probability distribution $p(\alpha|1e)$. [*Right, blue*]: The histogram of the S-spectrum slope α of the background (solar neutrino interaction), which is proportional to the conditional probability distribution $p(\alpha|2e)$. This two diagrams illustrate the differences in S_1 and α between signal off-center events and background off-center events

Chapter 3

Maximum likelihood estimation

3.1 Central events

Given an arbitrary central event, based on the approximation that different parameters $S_1(t_1)$, $S_1(t_2)$, $\alpha(t_1)$ and $\alpha(t_2)$ from different time bins t_1 and t_2 are not correlated (see Equation C.6 and C.7), the likelihood $p(2e|\vec{S}_{meas})$ for this event to be a signal event ($0\nu\beta\beta$, labeled as $2e$) is given by:

$$\begin{aligned} p(2e|\vec{S}_{meas}) &= \frac{p(\vec{S}_{meas}|2e)}{p(\vec{S}_{meas}|1e) + p(\vec{S}_{meas}|2e)} \\ &= \frac{p(S_1(t_1)|2e)p(S_1(t_2)|2e)p(\alpha(t_1)|2e)p(\alpha(t_2)|2e)}{\sum_{j=1}^{2} p(S_1(t_1)|je)p(S_1(t_2)|je)p(\alpha(t_1)|je)p(\alpha(t_2)|je)} \end{aligned} \tag{3.1}$$

Ideally, the likelihood $p(2e|\vec{S}_{meas})$ should be 0 for any background event, while it should be 1 for any signal event. However, in reality, there is inevitably a proportion of signal events that has low likelihood to be correctly classified as a signal event, and there is also inevitably a proportion of background events that has high likelihood to be falsely classified as a signal event. In specific, Figure 3.1 represents the distribution of such likelihood $p(2e|\vec{S}_{meas})$ of individual events.

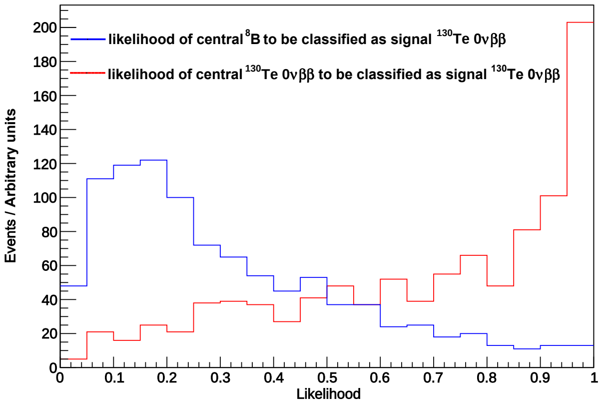

Figure 3.1: The likelihood distribution of the central events to be classified as signal ($0\nu\beta\beta$) events. *Red:* The likelihood distribution for the signal ($0\nu\beta\beta$) events to be correctly classified as the signal ($0\nu\beta\beta$) events. *Blue:* The likelihood distribution for the background (^{8}B) events to be falsely classified as the signal ($0\nu\beta\beta$) events. This diagram illustrates that the most events are correctly classified: the most background (^{8}B) events have relatively low likelihood to be wrongly classified as the signal ($0\nu\beta\beta$) events; the most signal ($0\nu\beta\beta$) events have relatively high likelihood to be correctly classified as the signal ($0\nu\beta\beta$) events. However, there is also some proportion of the signal ($0\nu\beta\beta$) and background (^{8}B) events are respectively wrongly classified as background (^{8}B) and signal ($0\nu\beta\beta$) events.

Introducing a likelihood threshold L_{cut}, one can conclude all the events with the likelihood $p(2e|\vec{S}_{meas})$ larger than L_{cut}, are signal events; meanwhile, one can also conclude all the events with the likelihood $p(2e|\vec{S}_{meas})$ smaller than L_{cut}, are background events.

Under such classification, there is a proportion among all the signal events that are correctly classified as signal events. Such proportion is defined to be the true positive rate (TPR), which is also known as signal efficiency. However, there is also a proportion among all the background events that are wrongly classified as signal events. Such proportion is defined to be the false positive rate (FPR). Moving around the likelihood threshold L_{cut} in the interval $[0, 1]$, one would get TPR(L_{cut}) and FPR(L_{cut}) as functions of the threshold L_{cut} over the interval $[0, 1]$ (see Figure 3.2).

The curve of TPR as a function of FPR is known as receiver operating characteristics (ROC). The area under the curve (AUC) of ROC characterizes how separated two distributions are. In this particular case, the AUC of central event classification is around 83.75%. The price of getting TPR (signal efficiency) of 70% is to have FPR around 19%.

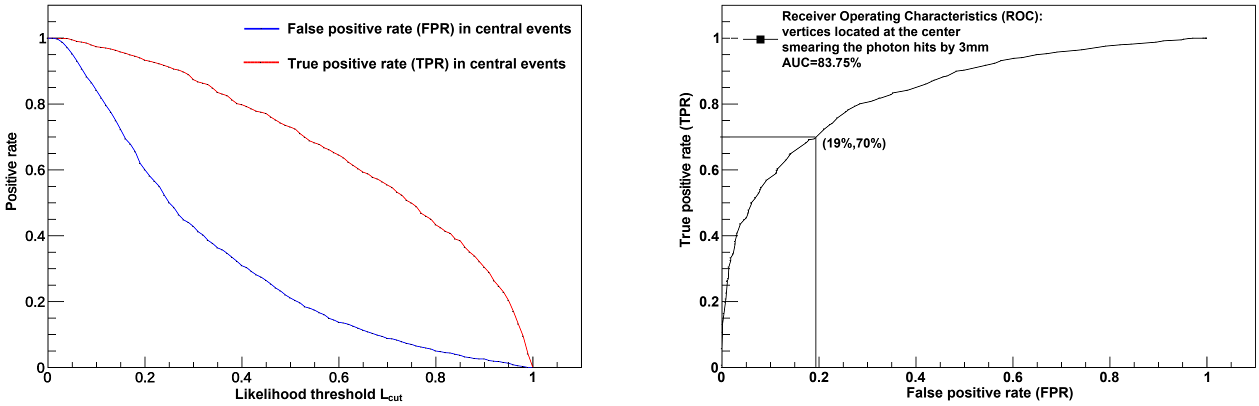

Figure 3.2: [*Left, Red*]: True positive rate TPR(L_{cut}) in the central events as a function of the likelihood threshold L_{cut}. [*Left, Blue*]: False positive rate FPR(L_{cut}) in the central events as a function of the likelihood threshold L_{cut}. [*Right*]: Receiver Operating Characteristics (ROC): eliminating the parameter L_{cut}, TPR(L_{cut}) as a function of FPR($L_c ut$). The area under the curve (AUC) of the ROC indicates the extent of the separation of any two distributions, which, in this particular case, are the likelihood distribution for a signal ($0\nu\beta\beta$) event to be correctly classified as a signal ($0\nu\beta\beta$) event, and the likelihood distribution for a background (^{8}B) event to be wrongly classified as a signal ($0\nu\beta\beta$) event. The more separated the two distributions are from each other, the larger the AUC of the ROC is. In the central event classification, we have achieved a 5.2 ^{8}B background suppression (defined to be $\frac{1}{FPR}$) at 70% $0\nu\beta\beta$-decay signal efficiency for events uniformly distributed throughout a 3 m radius fiducial volume.

3.2 Off-center events

In off-center event classification, because of the modification of the weight assignment $W(\theta, t)$ to each individual photon hit, all the photon hits are included and weighted accordingly. The parameter space is therefore simplified to be S_1 and α, because the photon hits are no longer split up into different time bins (such as t_1 and t_2 in the central event case).

Therefore, the likelihood $p(2e|\vec{S}_{meas})$ for an off-center event to be a signal event ($0\nu\beta\beta$, labeled as $2e$) is given by:

$$p(2e|\vec{S}_{meas}) = \frac{p(\vec{S}_{meas}|2e)}{p(\vec{S}_{meas}|1e) + p(\vec{S}_{meas}|2e)} = \frac{p(S_1|2e)p(\alpha|2e)}{\sum_{j=1}^{2} p(S_1|je)p(\alpha|je)} \tag{3.2}$$

Similar to the central event classification, introducing a likelihood threshold L_{cut}, one can plot TPR(L_{cut}) and FPR(L_{cut}) as functions of the threshold L_{cut}, and also plot TPR directly as a function of FPR by eliminating the parameter L_{cut} (See Figure 3.4). The curve of TPR as a function of FPR is the ROC, and the AUC of the ROC (which again characterizes how separated the two likelihood distributions are) in off-center event classification is around 71.72%. The price of getting TPR (signal efficiency) of 70% is to have FPR around 38% (background suppression $\frac{1}{FPR} = 263.16\%$).

In addition, for those $0\nu\beta\beta$ signals which were falsely classified as ^{8}B backgrounds, we can further separate them from the true backgrounds. We can compare the reconstructed electron direction $\hat{e}_{electron}$ (see Equation D.1) and Sun-Earth connection $\hat{e}_{SE}$. In true ^{8}B background events, the direction of the electron is more likely to be along the direction of the Sun-Earth connection $\hat{e}_{SE}$. However, in a $0\nu\beta\beta$-decay which is falsely classified as a ^{8}B background, the reconstructed direction of the electron should be equally likely to be at any solid angle. For example, the events with reconstructed electron direction $\hat{e}_{electron}$ opposite

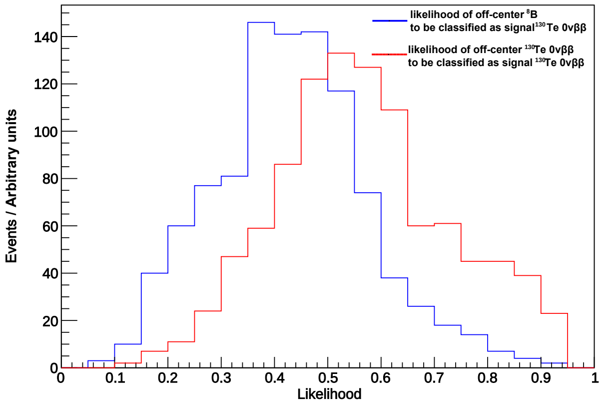

Figure 3.3: The likelihood distribution of the off-center events to be classified as the signal ($0\nu\beta\beta$) events. [*Red*]: The likelihood distribution for the signal ($0\nu\beta\beta$) events to be correctly classified as the signal ($0\nu\beta\beta$) events. [*Blue*]: The likelihood distribution for the background events (^{8}B) to be falsely classified as the signal ($0\nu\beta\beta$) events. This diagram illustrates that the most events are correctly classified: the most background (^{8}B) events have relatively low likelihood to be wrongly classified as the signal events ($0\nu\beta\beta$); the most signal ($0\nu\beta\beta$) events have relatively high likelihood to be correctly classified as the signal ($0\nu\beta\beta$) events. However, there is also some proportion of the signal ($0\nu\beta\beta$) and the background (^{8}B) events are respectively wrongly classified as the background (^{8}B) and the signal ($0\nu\beta\beta$) events.

to the Sun-Earth connection $\hat{e}_{SE}$ are more likely to be a $0\nu\beta\beta$ signal which was falsely classified as a ^{8}B background.

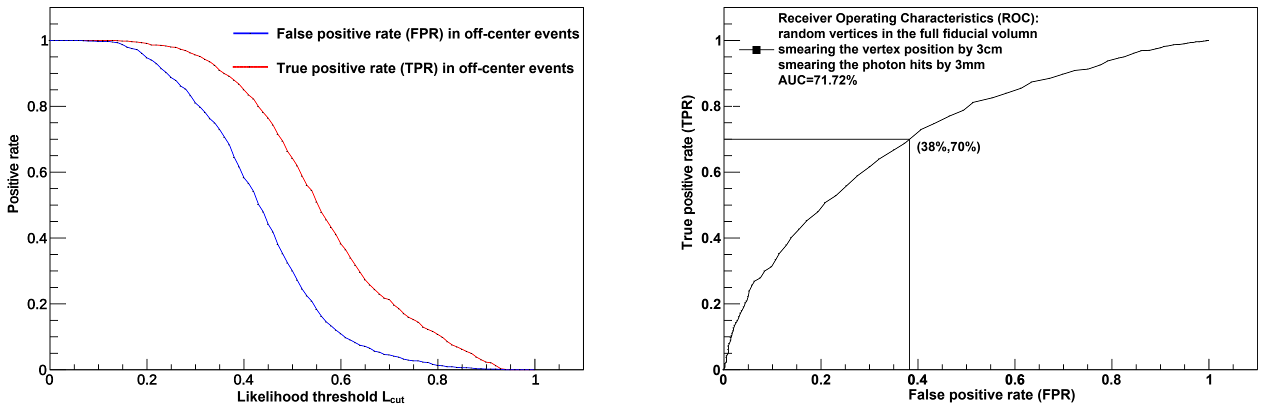

Figure 3.4: [*Left, Red*]: True positive rate (TPR) of the off-center events as a function TPR(L_{cut}) of the likelihood threshold L_{cut}. [*Left, Blue*]: False positive rate (FPR) of the off-center events as a function FPR(L_{cut}) of the likelihood threshold L_{cut}. [*Right*]: Receiver Operating Characteristics (ROC): eliminating the parameter L_{cut}, TPR(L_{cut}) as a function of FPR(L_{cut}). The area under the curve (AUC) of the ROC indicates the extent of separation between any two distributions, which, in this particular case, are the likelihood distribution for a signal event to be correctly classified as a signal event, and the likelihood distribution for a background event to be wrongly classified as a signal event. The AUC of the ROC is 71.72% in off-center event classification. In off-center event classification, we achieve a 2.6 ^{8}B background suppression (defined to be $\frac{1}{FPR}$) at 70% $0\nu\beta\beta$-decay signal efficiency for events uniformly distributed throughout a 3 m radius fiducial volume.

Chapter 4

Electron direction reconstruction

4.1 Electron direction reconstruction

For the events that are classified as background event, the reconstructed electron direction $\hat{e}_{electron}$ provides an extra handle to distinguish the signal events wrongly classified as background events, from the correctly classified background events. The electrons in the solar neutrino interaction are more likely to be scattered along the direction of the Sun-Earth connection $\hat{e}_{SE}$. Therefore, if the reconstructed electron direction $\hat{e}_{electron}$ of an event classified as a background, is opposite to the direction of the Sun-Earth connection $\hat{e}_{SE}$, such event becomes more likely to be a signal event that is wrongly classified as a background event.

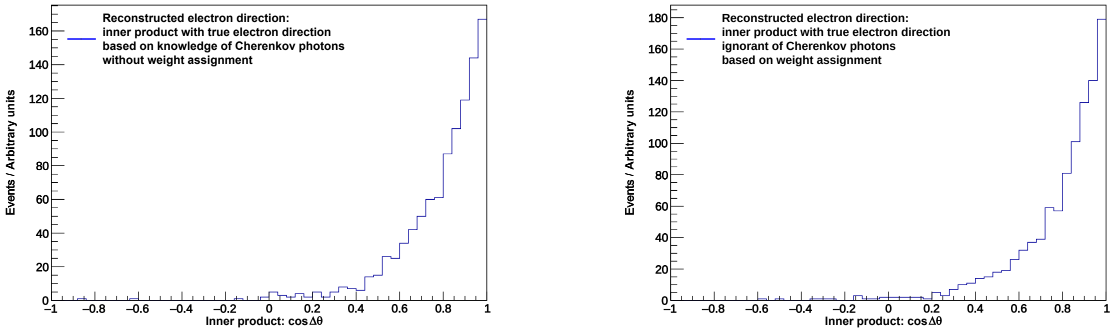

Figure 4.1: For off-center events, the reconstruction of the electron direction $\hat{e}_{electron}$ based on averaging over the (weighted unit) displacement vectors of each individual photon hit (within 4ns-9.5ns time bin after the first detected photon hit) from the reconstructed vertex. [*Left*]: Given the Cherenkov photon hits, but without assigning any weights to the individual photon hits, plotting the inner product $\cos\Delta\theta$ between the reconstructed electron direction and the true electron direction in a background event. [*Right*]: Without the knowledge of the Cherenkov photon hits, selecting all the photon with particular weight assignment $W(\theta, t)$, plotting the inner product $\cos\Delta\theta$ between the reconstructed electron direction and the true electron direction in a background event.

We have illustrated (see Figure 4.1) that the weight assignment function $W(\theta, t)$ has a positive contribution to the electron direction $\hat{e}_{electron} = \frac{\sum_i^{N_{PE}} W(\theta_i,t_i)\frac{\vec{r}_i-\vec{r}_v}{|\vec{r}_i-\vec{r}_v|}}{\left|\sum_i^{N_{PE}} W(\theta_i,t_i)\frac{\vec{r}_i-\vec{r}_v}{|\vec{r}_i-\vec{r}_v|}\right|}$ (see Equation D.1), which makes the reconstructed electron direction even more accurate than only specifying the N_{Ch} cherenkov photons without any weight assignment: $\hat{e}_{electron} = \frac{\sum_i^{N_{Ch}} \frac{\vec{r}_i-\vec{r}_v}{|\vec{r}_i-\vec{r}_v|}}{\left|\sum_i^{N_{Ch}} \frac{\vec{r}_i-\vec{r}_v}{|\vec{r}_i-\vec{r}_v|}\right|}$. The reason behind such improvement in the Figure 4.1 is that the weight assignment mitigates the negative impact of electron multiple scattering on electron direction reconstruction. For the same given destination (i.e., a particular detector), the Cherenkov photons emitted from the electron, that has experienced multiple scattering, arrive later than the Chrenkov photons emitted from the same electron that has not yet experienced multiple scattering. Therefore, the weight assignment function $W(\theta, t)$ assigns much more weights on the Cherenkov photons from the electron that is not yet multiple-scattered; while the method assigns much less weights on the Cherenkov photons from the electron that is already multiple scattered. As a consequence, the reconstructed electron direction becomes more accurate after assigning a weight $W(\theta, t)$ to each individual photon hit $\frac{\delta(\theta-\theta_i)\delta(\phi-\phi_i)}{\sin\theta_i}$.

Chapter 5

Conclusion

5.1 Conclusion

Based on the use of the large-area picosecond photodetectors (LAPPD) with a spatial resolution less than 1mm[1] and a time resolution of 100 ps, we simulated the signal events ($0\nu\beta\beta$-decays) and the background events (^{8}B solar neutrino interactions) in a liquid scintillator detector with the radius of 6.5 m.

The previous research [15] has proposed a technique to separate the signal events from the background events with the spherical harmonics analysis. In this paper, we have improved the technique by harnessing all the spacetime coordinates of each individual PE, modifying the integral into a summation to calculate the S-spectrum S_ℓ, and assigning more weights on the Cherenkov photons than the scintillation photons.

For the events simulated with the vertices at the center of the detector sphere, we have achieved a background suppression factor of 5.2 at 70% signal efficiency. In comparison, the previous method [15] for the central events achieved a background suppression factor of 4.5 at 70% signal efficiency.

For the events simulated with the vertices randomly generated uniformly throughout the fiducial volume with the 3 m radius, we have achieved a background suppression factor of 2.6 at 70% signal efficiency. This new level of background suppression was previously [15] achieved only by increasing the risetime of the scintillation light from 1 ns to 5 ns. In direct comparison, without any modification of the scintillator risetime, the previous method in the off-center events achieved a background suppression factor of 2.0 at 70% signal efficiency.

The improved spherical harmonics analysis enhances the computation speed by more than a factor of 200, because the summation form of the S-spectrum has simplified the calculation of the two-dimensional integrals.

In addition, we have completed the first simulation studies demonstrating the direction reconstruction of the 2.5 MeV electrons in a liquid scintillator detector for events uniformly distributed in the R<3 m fiducial volume. Supplementary to using only event topology, reconstructing the electron direction and correlating the electron direction with the position of the sun may help to further suppress the ^{8}B background in the off-center events.

We have also proposed a potential vertex reconstruction scheme, based on harnessing the hit positions of the scintillation photons, supplementary to the vertex reconstruction scheme based on the hit positions of the Cherenkov photons in the previous research.

---

[1] In this paper, we smeared the hit positions of the PE's by 3 mm to be conservative.

Appendix A

Spherical harmonics analysis

A.1 S-spectrum S_l

Suppose the angular distribution $f(\theta,\phi)$ over the unit sphere S^2 represents the angular distribution of photo-electrons (PE) over the detector surface. Such angular distribution $f(\theta,\phi)$ has its corresponding spherical harmonics expansion:

$$f(\theta,\phi) = \sum_{\ell=0}^{+\infty} \sum_{m=-\ell}^{\ell} f_{\ell m} Y_{\ell m}(\theta,\phi) \tag{A.1}$$

where $Y_{\ell m}(\theta,\phi)$ are tesseral harmonics (real-valued spherical harmonics), which form a complete orthonormal basis of the rigged Hilbert space (all real square integrable functions and Dirac delta functions defined over S^2):

$$Y_{\ell m}(\theta,\phi) = \begin{cases} \sqrt{2}\sqrt{\frac{(2\ell+1)}{4\pi}\frac{(\ell-m)!}{(\ell+m)!}}P_\ell^m(\cos\theta)\cos\ m\phi & ,\text{if } m > 0 \\ \sqrt{\frac{(2\ell+1)}{4\pi}\frac{(\ell-m)!}{(\ell+m)!}}P_\ell^m(\cos\theta) & ,\text{if } m = 0 \\ \sqrt{2}\sqrt{\frac{(2\ell+1)}{4\pi}\frac{(\ell-m)!}{(\ell+m)!}}P_\ell^{|m|}(\cos\theta)\sin\ |m|\phi & ,\text{if } m < 0 \end{cases} \tag{A.2}$$

and the projection coefficients $f_{\ell m}$ are given by the projection of $f(\theta,\phi)$ onto the basis $Y_{\ell m}(\theta,\phi)$:

$$f_{\ell m} = \int_0^\pi \sin\theta d\theta \int_0^{2\pi} d\phi f(\theta,\phi) Y_{\ell m}(\theta,\phi) \tag{A.3}$$

For a given angular distribution $f(\theta,\phi)$, its rotational invariant S-spectrum S_ℓ is therefore:

$$S_\ell = \sum_{m=-\ell}^{\ell} |f_{\ell m}|^2 \tag{A.4}$$

A.2 Angular Distribution $f(\theta,\phi)$ of photo-electrons

Suppose the Dirac delta function $\frac{\delta(\theta-\theta_i)\delta(\phi-\phi_i)}{\sin\theta_i}$ represents the angular distribution of an individual PE at (θ_i,ϕ_i) on the detector surface. Therefore, the L^1-normalized (see Equation A.8) angular distribution $f(\theta,\phi)$ of N_{PE} photo-electrons (PE) is

$$f(\theta,\phi) = \frac{1}{N_{PE}} \sum_{i=1}^{N_{PE}} \frac{\delta(\theta-\theta_i)\delta(\phi-\phi_i)}{\sin\theta_i} \tag{A.5}$$

Substituting the distribution $f(\theta,\phi)$ into the Equation A.3 yields the projection coefficients $f_{\ell m}$:

$$f_{\ell m} = \sum_{i=1}^{N_{PE}} \int_0^{\pi} d\theta \int_0^{2\pi} d\phi \frac{\sin\theta}{\sin\theta_i} \delta(\theta-\theta_i)\delta(\phi-\phi_i) \frac{Y_{\ell m}(\theta,\phi)}{N_{PE}} = \sum_{i=1}^{N_{PE}} \frac{Y_{\ell m}(\theta_i,\phi_i)}{N_{PE}} \tag{A.6}$$

and also its S-spectrum S_ℓ:

$$S_\ell = \sum_{m=-\ell}^{\ell} |f_{\ell m}|^2 = \frac{1}{N_{PE}^2} \sum_{m=-\ell}^{\ell} \left| \sum_{i=1}^{N_{PE}} Y_{\ell m}(\theta_i,\phi_i) \right|^2 \tag{A.7}$$

A.3 Normalization of the Angular Distribution $f(\theta,\phi)$

In this paper, the angular distribution $f(\theta,\phi)$ of the photo-electrons is normalized by the L^1 norm:

$$||f(\theta,\phi||_1 = \int_{S^2} d\Omega |f(\theta,\phi)| \tag{A.8}$$

For example, the L^1 norm of the angular distribution $f(\theta,\phi) = \sum_{i=1}^{N_{PE}} \frac{\delta(\theta-\theta_i)\delta(\phi-\phi_i)}{\sin\theta_i}$, which is not yet normalized, is N_{PE}. As a consequence, in this paper, all the S-spectra has the normalization factor N_{PE}^2 in the denominator.

Note, in principle, the sum of S_ℓ's over all multiple moments ℓ equals to the L^2 norm of the function $f(\theta,\phi)$:

$$||f(\theta,\phi||_2 = \int_{S^2} d\Omega |f(\theta,\phi)|^2 = \sum_{\ell=0}^{+\infty} S_\ell \tag{A.9}$$

However, the detection signal $f(\theta,\phi)$ in this paper, which is the sum of the Dirac delta functions $\sum_{i=1}^{N_{PE}} \frac{\delta(\theta-\theta_i)\delta(\phi-\phi_i)}{\sin\theta_i}$, is not square integrable; therefore, the sum of S_ℓ's diverges.

A.4 the S-spectrum of idealized central events with uniform Scintillation background

Suppose the vertex of the solar neutrino interaction is at the center of the detector sphere, then the angular distribution $f(\theta,\phi)$ of the photo-electrons looks like a ring distributed over the sphere. Since the S-spectrum S_l is rotational invariant, one can calculate S_l with z-axis aligned with the direction of the electron motion.

Therefore, under such definition of the coordinate system, the idealized PE angular distribution $f(\theta,\phi)$ of a solar neutrino interaction event is

$$f(\theta,\phi) = \frac{\delta(\theta-\theta_c)}{2\pi\sin\theta_c} \tag{A.10}$$

where θ_c is the Cherenkov angle.

Substituting such idealized angular distribution $f(\theta,\phi)$ into Equation A.3, one can derive its projection coefficients $f_{\ell m}$:

$$
\begin{aligned}
f_{\ell m} &= \int_0^{\pi} \sin\theta d\theta \int_0^{2\pi} d\phi f(\theta,\phi) Y_{\ell m}(\theta,\phi) \\
&= \int_0^{\pi} \sin\theta d\theta \int_0^{2\pi} d\phi \frac{\delta(\theta-\theta_c)}{2\pi\sin\theta_c} Y_{\ell m}(\theta,\phi) \\
&= \begin{cases}
\int_0^{\pi} \sin\theta d\theta \int_0^{2\pi} d\phi \frac{\delta(\theta-\theta_c)}{2\pi\sin\theta_c} \sqrt{2}\sqrt{\frac{(2\ell+1)}{4\pi}\frac{(\ell-m)!}{(\ell+m)!}} P_\ell^m(\cos\theta)\cos\ m\phi & \text{, if } m>0 \\
\int_0^{\pi} \sin\theta d\theta \int_0^{2\pi} d\phi \frac{\delta(\theta-\theta_c)}{2\pi\sin\theta_c} \sqrt{\frac{(2\ell+1)}{4\pi}\frac{(\ell-m)!}{(\ell+m)!}} P_\ell^m(\cos\theta) & \text{, if } m=0 \\
\int_0^{\pi} \sin\theta d\theta \int_0^{2\pi} d\phi \frac{\delta(\theta-\theta_c)}{2\pi\sin\theta_c} \sqrt{2}\sqrt{\frac{(2\ell+1)}{4\pi}\frac{(\ell-m)!}{(\ell+m)!}} P_\ell^{|m|}(\cos\theta)\sin\ |m|\phi & \text{, if } m<0
\end{cases} \\
&= \begin{cases}
0 & \text{, if } m>0 \\
\int_0^{\pi} \sin\theta d\theta \frac{\delta(\theta-\theta_c)}{\sin\theta_c}\sqrt{\frac{(2\ell+1)}{4\pi}} P_\ell(\cos\theta) = \sqrt{\frac{(2\ell+1)}{4\pi}} P_\ell(\cos\theta_c) & \text{, if } m=0 \\
0 & \text{, if } m<0
\end{cases}
\end{aligned}
\tag{A.11}
$$

Consequently, the S-spectrum S_ℓ of the idealized PE angular distribution $f(\theta,\phi)$ of the solar neutrino interaction from the center of the detector sphere is given by:

$$
S_\ell = \sum_{m=-\ell}^{\ell} |f_{\ell m}|^2 = \frac{(2\ell+1)}{4\pi}[P_\ell(\cos\theta_c)]^2 \tag{A.12}
$$

The idealized PE angular distribution $f(\theta,\phi)$ of a $0\nu\beta\beta$ event with its vertex at the center of the detector sphere is:

$$
f(\theta,\phi) = \frac{1}{2}\frac{\delta(\theta-\theta_c)}{2\pi\sin\theta_c} + \frac{1}{2}\frac{\delta(\theta-(\pi-\theta_c))}{2\pi\sin\theta_c} \tag{A.13}
$$

The S-spectrum of the idealized PE angular distribution $f(\theta,\phi)$ of the $0\nu\beta\beta$ event can be similarly be derived:

$$
f_{\ell m} = \frac{1}{2}\sqrt{\frac{(2\ell+1)}{4\pi}}[P_\ell(\cos\theta_c) + P_\ell(-\cos\theta_c)] \tag{A.14}
$$

$$
\begin{aligned}
S_\ell &= \sum_{m=-\ell}^{\ell} |f_{\ell m}|^2 = \sum_{m=-\ell}^{\ell} \left| \frac{1}{2}\sqrt{\frac{(2\ell+1)}{4\pi}}[P_\ell(\cos\theta_c) + P_\ell(-\cos\theta_c)] \right|^2 \\
&= \begin{cases}
0 & \text{, if } \ell\ odd \\
\frac{(2\ell+1)}{4\pi}[P_\ell(\cos\theta_c)]^2 & \text{, if } \ell\ even
\end{cases}
\end{aligned}
\tag{A.15}
$$

A.5 S-spectrum in the special cases of the off-center events

Suppose the vertex of an off-center event is displaced by $\vec{r}_v$ along the z-axis from the center of the detector sphere, and suppose the direction of the electron in this event is either parallel or opposite to the vertex displacement vector $\vec{r}_v$. Then the angular distribution of the Cherenkov photon hits over the sphere is given by one of the following in a solar neutrino interaction event (or a half of the sum of the both in a $0\nu\beta\beta$ event):

$$\begin{cases} f_1(\theta,\phi) = \frac{\delta(\cos\theta - \cos\theta_1)}{2\pi} & ,\theta_1 < \frac{\pi}{2} \\ f_2(\theta,\phi) = \frac{\delta(\cos\theta - \cos\theta_2)}{2\pi} & ,\theta_2 > \frac{\pi}{2} \end{cases} \tag{A.16}$$

The angles θ_1 and θ_2 are constrained by simple geometry:

$$\begin{cases} R\cos\theta_1 - r = R\sin\theta_1\cot\theta_c & ,\theta_1 < \frac{\pi}{2} \\ r - R\cos\theta_2 = R\sin\theta_2\cot\theta_c & ,\theta_2 > \frac{\pi}{2} \end{cases} \tag{A.17}$$

The solution to the equation above is given by:

$$\begin{cases} \cos\theta_1 = \sin^2\theta_c\frac{r_0}{R} + cos\theta_c\sqrt{1-\sin^2\theta_c\frac{r_0^2}{R^2}} \\ \cos\theta_2 = \sin^2\theta_c\frac{r_0}{R} - cos\theta_c\sqrt{1-\sin^2\theta_c\frac{r_0^2}{R^2}} \end{cases} \tag{A.18}$$

Therefore, in this special solar neutrino interaction event, the S-spectrum S_ℓ is given by either of the following, depending on whether the direction of the electron $\hat{e}_{electron}$ is along with (then θ_1) or opposite to (then θ_2) the direction of the vertex displacement vector $\hat{r}_v$:

$$\begin{cases} S_\ell = \frac{2\ell+1}{4\pi}[P_\ell(\cos\theta_1)]^2 \\ S_\ell = \frac{2\ell+1}{4\pi}[P_\ell(\cos\theta_2)]^2 \end{cases} \tag{A.19}$$

Similarly, in this special $0\nu\beta\beta$ event, the S-spectrum S_ℓ is given by:

$$S_\ell = \frac{(2\ell+1)}{16\pi}\sum_{m=-\ell}^{\ell}|P_\ell(\cos\theta_1) + P_\ell(\cos\theta_2)|^2 \tag{A.20}$$

A.6 S-spectrum in the general cases of the off-center events

Suppose the vertex of the solar neutrino interaction is at (x_v, y_v, z_v), from which the electron is produced and propagates towards any arbitrary direction. Because the S-spectrum S_l is invariant under rotation, we can pick the direction of the z-axis properly, which consumes the symmetry in θ, such that the direction of the electron is $\hat{e}_z$. In this coordinate system, the PE's are ideally distributed over the intersection between the Cherenkov cone and the detector sphere:

$$\begin{cases} r^2 - r_s^2 = 0 \\ (r\sin\theta\cos\phi - x_v)^2 + (r\sin\theta\sin\phi - y_v)^2 - (r\cos\theta - z_v)^2\tan^2\theta_c = 0 \end{cases} \tag{A.21}$$

where r_s is the radius of the detector sphere, θ_c is the Cherenkov angle.

For simplicity, define:

$$\begin{cases} \rho_v = \sqrt{x_v^2 + y_v^2} \\ \cos\phi_v = \frac{x_v}{\rho_v} \\ \sin\phi_v = \frac{y_v}{\rho_v} \end{cases} \tag{A.22}$$

Equations A.21 is therefore simplified to:

$$\begin{aligned}
0 &= (r_s \sin\theta \cos\phi - x_v)^2 + (r_s \sin\theta \sin\phi - y_v)^2 - (r_s \cos\theta - z_v)^2 \tan^2\theta_c \\
&= (r_s^2 \sin^2\theta \cos^2\phi - 2x_v r_s \sin\theta \cos\phi + x_v^2) \\
&+ (r_s^2 \sin^2\theta \sin^2\phi - 2y_v r_s \sin\theta \sin\phi + y_v^2) \\
&- (r_s \cos\theta - z_v)^2 \tan^2\theta_c \\
&= r_s^2 \sin^2\theta - 2x_v r_s \sin\theta \cos\phi - 2y_v r_s \sin\theta \sin\phi + \rho_v^2 - (r_s \cos\theta - z_v)^2 \tan^2\theta_c
\end{aligned} \tag{A.23}$$

Assuming that $\rho_v \neq 0$, divide both sides by $2r_s\rho_v \sin\theta$:

$$\begin{aligned}
0 &= \frac{r_s^2 \sin^2\theta - 2x_v r_s \sin\theta \cos\phi - 2y_v r_s \sin\theta \sin\phi + \rho_v^2 - (r_s \cos\theta - z_v)^2 \tan^2\theta_c}{2r_s\rho_v \sin\theta} \\
&= \frac{r_s \sin\theta}{2\rho_v} - \frac{x_v \cos\phi}{\rho_v} - \frac{y_v \sin\phi}{\rho_v} + \frac{\rho_v}{2r_s \sin\theta} - \frac{(r_s \cos\theta - z_v)^2 \tan^2\theta_c}{2r_s\rho_v \sin\theta} \\
&= \frac{r_s \sin\theta}{2\rho_v} - \cos\phi_v \cos\phi - \sin\phi_v \sin\phi + \frac{\rho_v}{2r_s \sin\theta} - \frac{(r_s \cos\theta - z_v)^2 \tan^2\theta_c}{2r_s\rho_v \sin\theta} \\
\cos(\phi - \phi_v) &= \frac{r_s \sin\theta}{2\rho_v} + \frac{\rho_v}{2r_s \sin\theta} - \frac{(r_s \cos\theta - z_v)^2 \tan^2\theta_c}{2r_s\rho_v \sin\theta}
\end{aligned} \tag{A.24}$$

Using the relation between θ and ϕ, which describes the curve of the Cherenkov cone over the detector sphere, one could express the photon angular density distribution $f(\theta, \phi)$ and consequently the S-spectrum S_ℓ.

Appendix B

Separation of the Cherenkov/Scintillation photons and weight assignment function

B.1 Separation of Cherenkov/scintillation photons

For a general off-center event with its vertex displacement vector $\vec{r}_v$ along the z-axis, from the center of the detector sphere with radius R, suppose at time $\frac{R-r_v}{c(n)}$, the earliest scintillation photon arrives at the north pole of the detector sphere. In the later time bins, the scintillation photon hits start to spread symmetrically from the north pole. The time of the earliest scintillation photon arriving at any angle θ is therefore given by $\frac{\sqrt{R^2+r_v^2-2Rr_v\cos\theta}}{c(n)}$.

Due to the 1ns rise time of the earliest scintillation photons, all the Cherenkov photons must locate within the 1ns narrow band below the time boundary $t_{cut}(\theta)$ in the (θ, t) histogram (see Figure 2.4). Based on such fact, if the earliest photon is indeed a scintillation photon, the time boundary $t_{cut}(\theta)$ with respect to the earliest photon, which separates Cherenkov photons from the scintillation photons, is given by:

$$t_{cut}(\theta) = \frac{\sqrt{R^2+r_v^2-2Rr_v\cos\theta}}{c(n)} - \frac{R-r_v}{c(n)} \tag{B.1}$$

B.2 Scintillation Cone and the uncertainty of the time boundary

However, if there is any Cherenkov photon propagating towards the "vicinity" of the north pole, the earliest photon could be Cherenkov photon. In this case, suppose the earliest Cherenkov photon is t_{above} earlier than the earliest scintillation photon, then the earliest photon (which is a Cherenkov photon in this example) actually arrives at $\frac{R-r_v}{c(n)} - t_{above}$. Consequently, the time boundary t_{cut} with respect to the earliest photon becomes:

$$t_{cut}(\theta) = \frac{\sqrt{R^2+r_v^2-2Rr_v\cos\theta}}{c(n)} - \frac{R-r_v}{c(n)} + t_{above} \tag{B.2}$$

Intuitively, the uncertainty term t_{above} translates the entire time boundary $t_{cut}(\theta, t)$ upwards by t_{above}. For generality, in this paper, I kept the uncertainty term t_{above} explicit.

In addition, the so called "vicinity" of the north pole is actually a cone with a certain angle θ_s. For convenience, I suggest naming the cone with the term "scintillation cone" in this particular context. By definition of the scintillation cone with scintillation angle θ_s, if there is any Cherenkov photon enters such cone, which means the Cherenkov cone intersects with the scintillation cone, then the earliest photon will be Cherenkov photon.

Therefore, with the explicit definition of the scintillation cone and the scintillation angle θ_s, suppose the earliest scintillation photon starts Δt later than the earliest Cherenkov photon, one can calculate the scintillation angle θ_s of the scintillation cone based on the simple geometry:

$$\cos\theta_s = \frac{R^2 - r_v^2 - (R - r_v + c(n)\Delta t)^2}{2(R - r_v + c(n)\Delta t)r_v} \tag{B.3}$$

From the expression of $\cos_{\theta_s}$ above, we conclude that, the smaller the vertex displacement length r_v is, the larger the angle $theta_s$ is, the more likely the Cherenkov cone intersects with the scintillation cone, and therefore the more likely the earliest photon is a Cherenkov photon.

The conclusion above can also be drawn directly by inspecting the shape of the time boundary $t_{cut}(\theta) = \frac{\sqrt{R^2+r_v^2-2Rr_v\cos\theta}}{c(n)} - \frac{R-r_v}{c(n)}$. The smaller the vertex displacement length r_v is, the flatter the $t_{cut}(\theta)$ is, the more proportion of the Cherenkov narrow band is below the x-axis; therefore, the more likely there exists at least one Cherenkov photon below the x-axis, which is earlier than the earliest scintillation photon.

B.3 Weight assignment function

Despite knowing the probability of having Cherenkov photons earlier than the earliest scintillation photons by knowing the scintillation angle $\theta_s(r_v)$ as a function of vertex displacement length r_v, whether or not the earliest photon is a Cherenkov photon remains uncertain.

Therefore, it becomes necessary to design a weight assignment function $W(\theta, t)$ according to how early the photons are with respect to a "floating" time boundary $t_{cut}(\theta) = \frac{\sqrt{R^2+r_v^2-2Rr_v\cos\theta}}{c(n)} - \frac{R-r_v}{c(n)} + t_{above}$. By "floating", I mean the uncertainty term t_{above} is more or less a pure guess, which "floats" the entire time boundary upwards by t_{above}. The key of the weight assignment is to realize that, for a given angle θ the relative time difference Δt between the earliest Cherenkov photon and the earliest scintillation is fixed.

This means, regardless of the value of the uncertainty term t_{above}, we can design an exponential weight assignment function $W(\theta, t)$, such as:

$$W(\theta, t) = exp\left[\frac{\frac{\sqrt{R^2+r_v^2-2Rr_v\cos\theta}}{c(n)} - \frac{R-r_v}{c(n)} + t_{above} - t}{\tau}\right] \tag{B.4}$$

With such function, since the relative time difference between the earliest Cherenkov photon and the earliest scintillation photon is fixed to be a constant Δt for any given angle θ, the ratio of weight on the earliest Cherenkov photon to the earliest scintillation photon is also fixed to be a constant $e^{\frac{\Delta t}{\tau}}$.

B.4 Weighted detection signal and the modified S-spectrum

Assigning the weights $W(\theta_i, t_i)$ to the individual photon hits $\delta(\cos\theta - \cos\theta_i)\delta(\phi - \phi_i)$, the total L^1-normalized detection signal becomes:

$$f(\theta, \phi) = \frac{\sum_{i=1}^{N_{PE}} W(\theta_i, t_i)\delta(\cos\theta - \cos\theta_i)\delta(\phi - \phi_i)}{\sum_{i=1}^{N_{PE}} W(\theta_i, t_i)} \tag{B.5}$$

Simply substituting the modified photon hit angular density distribution $f(\theta, \phi)$ into the definition of the S-spectrum S_ℓ:

$$S_\ell = \sum_{m=-\ell}^{\ell} |f_{\ell m}|^2 = \sum_{m=-\ell}^{\ell} \frac{\left|\sum_{i=1}^{N_{PE}} W(\theta_i, t_i) Y_{\ell m}(\theta_i, \phi_i)\right|^2}{\left|\sum_{i=1}^{N_{PE}} W(\theta_i, t_i)\right|^2} \tag{B.6}$$

Appendix C

Maximum likelihood estimation

C.1 Conditional probability distribution

For an arbitrary event, given its measurement $\vec{S}_{meas}$ in the parameter space, the likelihood for the event to be a signal ($0\nu\beta\beta$, $2e$) is the conditional probability $p(1e|\vec{S}_{meas})$. Similarly, the likelihood for the event to be a background (solar neutrino interaction, $1e$) is the conditional probability $p(2e|\vec{S}_{meas})$. Based on Baysian theorem, these posterior probabilities are given by:

$$\begin{cases} p(1e|\vec{S}_{meas}) &= \frac{p(1e)}{p(\vec{S}_{meas})} p(\vec{S}_{meas}|1e) = k_1 p(\vec{S}_{meas}|1e) \\ p(2e|\vec{S}_{meas}) &= \frac{p(2e)}{p(\vec{S}_{meas})} p(\vec{S}_{meas}|2e) = k_2 p(\vec{S}_{meas}|2e) \end{cases} \tag{C.1}$$

where the response functions $p(\vec{S}_{meas}|1e)$ and $p(\vec{S}_{meas}|2e)$ are the conditional probability of getting measurement $\vec{S}_{meas}$ given the event is respectively a signal and a background, which can be read from the histograms in the Figure 2.3. The coefficients k_1 and k_2 are determined by the ratio of the prior probabilities $p(1e) : p(2e)$ and the normalization. In this paper, the ratio of the prior probabilities $k_1 : k_2 = p(1e) : p(2e)$ is set to be 1.

$$\begin{cases} k_1 : k_2 = p(1e) : p(2e) = 1 \\ k_1 p(\vec{S}_{meas}|1e) + k_2 p(\vec{S}_{meas}|2e) = 1 \end{cases} \tag{C.2}$$

Therefore, through solving the four equations in the Equation C.1 and C.2, the posterior probabilities $p(1e|\vec{S}_{meas})$ and $p(2e|\vec{S}_{meas})$ are given by

$$\begin{cases} p(1e|\vec{S}_{meas}) &= \frac{p(\vec{S}_{meas}|1e)}{p(\vec{S}_{meas}|1e)+p(\vec{S}_{meas}|2e)} \\ p(2e|\vec{S}_{meas}) &= \frac{p(\vec{S}_{meas}|2e)}{p(\vec{S}_{meas}|1e)+p(\vec{S}_{meas}|2e)} \end{cases} \tag{C.3}$$

C.2 multi-dimensional probability distribution

The probability distributions $p(s_1(t_1), s_1(t_2), \alpha(t_1), \alpha(t_2)|1e)$ and $p(s_1(t_1), s_1(t_2), \alpha(t_1), \alpha(t_2)|2e)$ can be directly applied to calculate the final likelihood and will probably yield slightly better result; however, it takes much more data than 1-dimensional case, to make such multi-dimensional probability distributions (which are essentially multi-dimensional histograms) more or less smooth. Given limited amount of data, the expedient applied in this paper is to replace these multi-dimensional histograms by the product of multiple 1-dimensional histograms (see Equation C.4).

C.3 Parameter space

For any central event, we can measure its S-spectrum S_ℓ and define the parameter space to be $\{S_\ell\}$, or for simplicity, define the parameter space to be $\{S_1, \alpha\}$, where α is the slope of the S-spectrum. In this paper, the parameter space is chosen to be $\{S_1(t_1), S_1(t_2), \alpha(t_1), \alpha(t_2)\}$, where t_1 and t_2 represents the first two time bins 0-1ns and 1-2ns with respect to the arrival time of the first detected photon.

On top of that, under the approximation that the parameters $S_1(t_1), S_1(t_2), \alpha(t_1), \alpha(t_2)$ are not correlated:

$$\begin{cases} p(S_1(t_1), S_1(t_2), \alpha(t_1), \alpha(t_2)|1e) \approx p(S_1(t_1)|1e)p(S_1(t_2)|1e)p(\alpha(t_1)|1e)p(\alpha(t_2)|1e) \\ p(S_1(t_1), S_1(t_2), \alpha(t_1), \alpha(t_2)|2e) \approx p(S_1(t_1)|2e)p(S_1(t_2)|2e)p(\alpha(t_1)|2e)p(\alpha(t_2)|2e) \end{cases} \tag{C.4}$$

the response functions $p(\vec{S}_{meas}|1e)$ and $p(\vec{S}_{meas}|2e)$ are therefore defined to be:

$$\begin{cases} p(\vec{S}_{meas}|1e) = p(S_1(t_1)|1e)p(S_1(t_2)|1e)p(\alpha(t_1)|1e)p(\alpha(t_2)|1e) \\ p(\vec{S}_{meas}|2e) = p(S_1(t_1)|2e)p(S_1(t_2)|2e)p(\alpha(t_1)|2e)p(\alpha(t_2)|2e) \end{cases} \tag{C.5}$$

we obtain the likelihoods:

$$\begin{cases} p(1e|\vec{S}_{meas}) &= \frac{p(S_1(t_1)|1e)p(S_1(t_2)|1e)p(\alpha(t_1)|1e)p(\alpha(t_2)|1e)}{N} \\ p(2e|\vec{S}_{meas}) &= \frac{p(S_1(t_1)|2e)p(S_1(t_2)|2e)p(\alpha(t_1)|2e)p(\alpha(t_2)|2e)}{N} \end{cases} \tag{C.6}$$

where the normalization factor N is given by

$$\begin{aligned} N &= p(S_1(t_1)|1e)p(S_1(t_2)|1e)p(\alpha(t_1)|1e)p(\alpha(t_2)|1e) \\ &\quad + p(S_1(t_1)|2e)p(S_1(t_2)|2e)p(\alpha(t_1)|2e)p(\alpha(t_2)|2e) \\ &= \sum_{j=1}^{2} p(S_1(t_1)|je)p(S_1(t_2)|je)p(\alpha(t_1)|je)p(\alpha(t_2)|je) \end{aligned} \tag{C.7}$$

C.4 Off-center events based on weight assignment

For the off-center event classification based on the weight assignment, we can plot the S-spectrum S_ℓ for each event and extract S_1 and the slope α of the S-spectrum S_ℓ. In this case, the maximum likelihood estimation is slightly easier, as the concept of time bin is removed and all the photons are included. Therefore, there are only two parameters S_1 and the slope α for off-center event classification. Despite the difference in the time bin, the off-center event classification is similar to the center event classification, and the specific likelihood is given by

$$p(2e|\vec{S}_{meas}) = \frac{p(\vec{S}_{meas}|2e)}{p(\vec{S}_{meas}|1e) + p(\vec{S}_{meas}|2e)} = \frac{p(S_1|2e)p(\alpha|2e)}{\sum_{j=1}^{2} p(S_1|je)p(\alpha|je)} \tag{C.8}$$

Appendix D

Event reconstruction

D.1 Vertex displacement direction reconstruction

If we define the z-axis of the spherical coordinate system to be aligned with the vertex displacement direction, the scintillation photon will arrive at the north pole of the detector sphere. After a small amount of time, the early scintillation photon hits will start to spread symmetrically from the north pole over the detector sphere.

Because of the symmetry of the scintillation photon hits over the detector sphere, the center of mass of the early scintillation photon hits (at this point all early photons are weighted equally) must be along the direction $\hat{r}_v$ of the vertex displacement vector $\vec{r}_v$, which will be defined to be aligned the z-axis.

Furthermore, after the rise time of the liquid scintillator, with respect to the first photon hit on the detector sphere, the scintillation photon hits start to become dominant relative to the Cherenkov photon hits. Therefore, we can use the photon hits within the time bin of 4ns-9.5ns after the first photon hit to reconstruct the center of mass of the early scintillation photons.

Consequently, we reconstructed the direction $\hat{r}_v$ of the vertex displacement vector $\vec{r}_v$ and redefined the spherical coordinates of all the photon hits, such that the redefined z-axis is aligned with the direction $\hat{r}_v$ of the reconstructed vertex displacement vector $\vec{r}_v$.

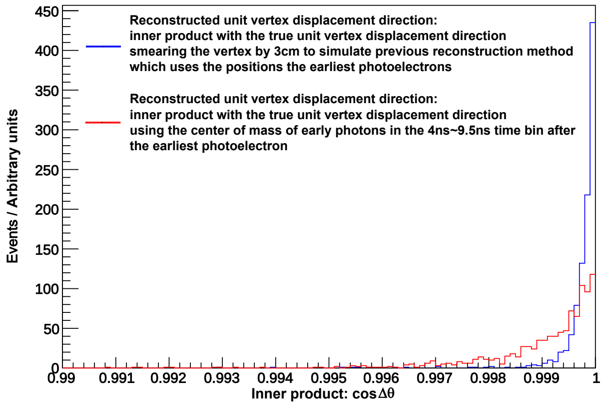

Figure D.1: The horizontal axis represents the inner product of the direction of the reconstructed vertex displacement vector and the direction of the true vertex displacement vector. The vertical axis represents the density of events that have the corresponding inner product of the directions. [*Blue*]: Vertex Displacement Direction $\hat{r}_v$ reconstruction based on our previous research using the early Cherenkov photons. [*Red*]: Vertex Displacement Direction $\hat{r}_v$ reconstruction based on the new technique using the early scintillation photons.

Potentially, we can combine both the method in the previous paper and the method proposed in this paper to reconstruct the vertex displacement direction with a higher accuracy.

D.2 Vertex displacement length reconstruction

There are two potential methods to reconstruct the vertex displacement length r_v on top of reconstructing the vertex displacement direction $\hat{r}_v$, which are both aiming to reconstruct the time boundary $t_{cut}(\theta)$ first. Because the time boundary $t_{cut}(\theta)$ is essentially a parametric function of θ, with parameter r_v (which is length of the vertex displacement vector $\vec{r}_v$, see Equation 2.3), the parameter r_v can therefore be extracted from the reconstructed time boundary $t_{cut}(\theta)$.

The first proposed method is based on the scintillation photon hit peak (peak over the arrival time t domain) for each angle θ. Given any angle θ on the detector, the scintillation photon hit per unit time reaches the peak, 3ns after the first scintillation photon. Therefore, recognizing the time $t_{peak}(\theta)$ of the scintillation peak for each angle θ, and translate the peak by 3ns will give us the time boundary: $t_{cut}(\theta) = t_{peak}(\theta) - 3$ (in the unit of ns).

The second proposed method is based on the proper selection of the early photons for each angle θ. For each θ bin, we can pick some number of the earliest photon hits in the bin. The more hits we include, the more likely these photons are early scintillation photons. Averaging over the arrival time of these selected photons yields a estimated time boundary $t_{cut}(\theta)$ for each θ bin.

These two methods might also be combined and generalized by plotting the arrival time of each θ bin and then reconstructing the early scintillation time boundary $t_{cut}(\theta)$.

D.3 Electron direction reconstruction

Let $\vec{r}_i$ represent the displacement vector of the i^{th} photon hit from the center of the detector sphere, and again let $\vec{r}_v$ represent the displacement vector of the vertex from the center of the detector sphere.

Therefore, the vector $(\vec{r}_i - \vec{r}_v)$ represents the displacement vector of the i^{th} photon hit from the vertex of this event, and the vector $\frac{\vec{r}_i-\vec{r}_v}{|\vec{r}_i-\vec{r}_v|}$ represents the unit displacement vector of the i^{th} photon hit from the vertex of this event.

To reconstruct the direction of the electron in an off-center event, we assigned the weight $W(\theta, t)$ to each individual photon in order to exponentially increase the total weight of the Cherenkov photon hits and to exponentially suppress the total weight of the scintillation photon hits.

Assume that we have sufficient number of the Cherenkov photons, such that at any instance the photon hits are relatively uniformly distributed over the Cherenkov ring over the detector sphere. If the number of the Cherenkov photons is not sufficient, the Cherenkov photons at different time could be distributed unevenly over the Cherenkov ring on the detector sphere. Under the assumption of sufficient Cherenkov photons, the exponentially unequal weights $W(\theta, t)$ assigned to different time does not hurt the uniformity of the Cherenkov photon distribution over the Cherenkov ring over the detector sphere.

Therefore, the electron direction $\hat{e}_{electron}$ is the normalized sum of the weighted unit displacement vector of the i^{th} photon hit from the vertex of this event:

$$\hat{e}_{electron} = \frac{\sum_i^{N_{PE}} W(\theta_i, t_i) \frac{\vec{r}_i-\vec{r}_v}{|\vec{r}_i-\vec{r}_v|}}{\left| \sum_i^{N_{PE}} W(\theta_i, t_i) \frac{\vec{r}_i-\vec{r}_v}{|\vec{r}_i-\vec{r}_v|} \right|} \tag{D.1}$$

D.4 Multiple vertices

We propose a potential method regarding to the number of the vertices in an off-center event, based on checking the reconstructed time boundary $t_{cut}(\theta)$ or $t_{cut}(\theta, \phi)$.

If the number of the vertices in an event is more than one (for instance, there could be multiple electrons that are Compton scattered by high energy gamma rays), the time boundary $t_{cut}(\theta)$ of the photon hit distribution over (θ, t) will not have the same shape as we presented: $t_{cut}(\theta) = \frac{\sqrt{R^2+r_v^2-2Rr_v\cos\theta}}{c(n)} - \frac{R-r_v}{c(n)} + t_{above}$.

Instead, the expression of the boundary in this case will be the superposition of the time boundaries of different vertices. The superposed time boundary takes the earliest time boundary for each angle (θ, ϕ), which should potentially be recognized by checking the time boundary $t_{cut}(\theta)$ or $t_{cut}(\theta, \phi)$ of this event. The more separated the vertices are, the more different the shape of the plotted time boundary $t_{cut}(\theta)$ is from the presented one, and the more likely the number of the vertices is more than one.

Bibliography

[1] Ettore Majorana. In: *Nuovo Cim.* 14 (1937), pp. 171–184. DOI: 10.1007/BF02961314.

[2] M. Fukugita and T. Yanagida. “Barygenesis without grand unification”. In: *Phys. Lett. B* 174.1 (1986), pp. 45 –47. ISSN: 0370-2693. DOI: http://dx.doi.org/10.1016/0370-2693(86)91126-3. URL: http://www.sciencedirect.com/science/article/pii/0370269386911263.

[3] S. F. King. “Neutrino mass models”. In: *Rept. Prog. Phys.* 67 (2004), pp. 107–158. DOI: 10.1088/0034-4885/67/2/R01. arXiv: hep-ph/0310204 [hep-ph].

[4] M. Goeppert-Mayer. In: *Phys. Rev.* 48 (1935), pp. 512–516. DOI: 10.1103/PhysRev.48.512.

[5] W. H. Furry. In: *Phys. Rev.* 56 (12 1939), pp. 1184–1193.

[6] Michael Duerr. “Lepton number violating new physics and neutrinoless double beta decay”. In: *Nucl. Phys. Proc. Suppl.* 237-238 (2013), pp. 24–27. DOI: 10.1016/j.nuclphysbps.2013.04.048.

[7] J. Schechter and J. W. F. Valle. “Neutrinoless Double beta Decay in SU(2) x U(1) Theories”. In: *Phys. Rev.* D25 (1982). [,289(1981)], p. 2951. DOI: 10.1103/PhysRevD.25.2951.

[8] Michael Duerr, Manfred Lindner, and Alexander Merle. “On the Quantitative Impact of the Schechter-Valle Theorem”. In: *JHEP* 06 (2011), p. 091. DOI: 10.1007/JHEP06(2011)091. arXiv: 1105.0901 [hep-ph].

[9] J. B. Albert et al. “Search for Majorana neutrinos with the first two years of EXO-200 data”. In: *Nature* 510 (2014), pp. 229–234. DOI: 10.1038/nature13432. arXiv: 1402.6956 [nucl-ex].

[10] A. Gando et al. “Search for Majorana Neutrinos near the Inverted Mass Hierarchy Region with KamLAND-Zen”. In: *Phys. Rev. Lett.* 117.8 (2016). [Addendum: Phys. Rev. Lett.117,no.10,109903(2016)], p. 082503. DOI: 10.1103/PhysRevLett.117.109903, 10.1103/PhysRevLett.117.082503. arXiv: 1605.02889 [hep-ex].

[11] M. Agostini et al. “Improved Limit on Neutrinoless Double-β Decay of ^{76}Ge from GERDA Phase II”. In: *Phys. Rev. Lett.* 120 (13 2018), p. 132503. DOI: 10.1103/PhysRevLett.120.132503. URL: https://link.aps.org/doi/10.1103/PhysRevLett.120.132503.

[12] *2015 NSAC Long Range Plan*. 2015. URL: http://science.energy.gov/~/media/np/nsac/pdf/2015LRP/2015_LRPNS_091815.pdf.

[13] S. D. Biller. In: *Phys. Rev. D* 87.7, 071301 (Apr. 2013), p. 071301.

[14] S. Andringa et al. “Current Status and Future Prospects of the SNO+ Experiment”. In: *Adv. High Energy Phys.* 2016 (2016), p. 6194250. DOI: 10.1155/2016/6194250. arXiv: 1508.05759 [physics.ins-det].

[15] Andrey Elagin et al. “Separating Double-Beta Decay Events from Solar Neutrino Interactions in a Kiloton-Scale Liquid Scintillator Detector By Fast Timing”. In: *Nucl. Instrum. Meth.* A849 (2017), pp. 102–111. DOI: 10.1016/j.nima.2016.12.033. arXiv: 1609.09865 [physics.ins-det].

[16] L Winslow and R Simpson. “Characterizing quantum-dot-doped liquid scintillator for applications to neutrino detectors”. In: *Journal of Instrumentation* 7 (2012), P07010. URL: http://stacks.iop.org/1748-0221/7/i=07/a=P07010.

[17] C. Aberle et al. In: *J. Instrum.* 9.06 (2014), P06012.

[18] J. R. Alonso et al. In: *arXiv* 1409.5864 (2014). arXiv: 1409.5864 [physics.ins-det].

[19] J. Caravaca et al. “Cherenkov and Scintillation Light Separation in Organic Liquid Scintillators”. In: *Eur. Phys. J.* C77.12 (2017), p. 811. DOI: `10.1140/epjc/s10052-017-5380-x`. arXiv: `1610.02011 [physics.ins-det]`.

[20] Mohan Li et al. In: *Nucl. Instrum. Meth.* A830 (2016), pp. 303–308. DOI: `10.1016/j.nima.2016.05.132`. arXiv: `1511.09339 [physics.ins-det]`.

[21] R. Pordes et al. “The open science grid”. In: *Journal of Physics: Conference Series* 78.1 (2007), p. 012057. URL: `http://stacks.iop.org/1742-6596/78/i=1/a=012057`.

[22] Igor Sfiligoi et al. “The pilot way to Grid resources using glideinWMS”. In: *WRI World Congress* 2 (2009), pp. 428–432. DOI: `10.1109/CSIE.2009.950`.

[23] Bernhard Adams et al. In: *Nucl.Instrum.Meth.* A795 (2015), pp. 1–11. DOI: `doi:10.1016/j.nima.2015.05.027`.